Non-affine motion and selection of slip coefficient in constitutive modelling of polymeric solutions using a mixed derivative

D. Nieto Simavilla,[1,2] P. Español,[3] and M. Ellero[2,4,5]
[1)]*Dept. Energía y Combustibles, Escuela Técnica Superior de Ingenieros de Minas y Energía, Universidad Politécnica de Madrid, Calle Alenza 4, E-28011 Madrid, Spain*
[2)]*Basque Center for Applied Mathematics (BCAM), Alameda Mazarredo 14, E-48009 Bilbao, Vizcaya, Spain*
[3)]*Dept. Física Fundamental, Universidad Nacional de Educación a Distancia, Aptdo. 60141, E-28080 Madrid, Spain*
[4)]*IKERBASQUE, Basque Foundation for Science, Calle María Díaz de Haro 3, E-48013, Vizcaya, Spain*
[5)]*Zienkiewicz Centor for Computational Engineering (ZCCE), Swansea University, Bay Campus, SA1 8EN Swansea, United Kingdom*

(*Electronic mail: david.nsimavilla@upm.es)

(Dated: 21 October 2022)

Constitutive models for the dynamics of polymer solutions traditionally rely on closure relations for the extra stress, or related microstructural variables (e.g., conformation tensor) linking them to flow history. In this work, we study the eigendynamics of the conformation tensor within the GENERIC framework in mesoscopic computer simulations of polymer solutions to separate the effects of the non-affine motion from other sources of non-Newtonian behaviour. We observe that non-affine motion or slip increases with both, the polymer concentration, and the polymer chain length. Our analysis allows to uniquely calibrate a mixed derivative of the Gordon-Schowalter type in macroscopic models based on a micro-macro mapping of the dynamics of the polymeric system. The presented approach paves the way for better polymer constitutive modelling in multiscale simulations of polymer solutions, where different sources of non-Newtonian behaviour are modelled independently.

I. INTRODUCTION

Polymeric solutions display complex rheological behavior when subjected to flow. This is a direct result of additional contributions to stress given by the stretching and orientation of the polymer chains immersed in the fluid. Multiscale schemes are an extremely attractive solution for the simulation of these and other complex fluids. These schemes aim to simulate real flow processes without paying all the computational cost required to resolve the microscopic details.[1] The data from microscopic scale simulations can be used to obtain the closure constitutive relations needed to solve the macroscopic scale flow and obtain, for example, the viscosity or normal stresses as a function of the shear rate in a flowing polymeric solution.[2] The most naive approach is to simply fit the simulation data with some phenomenological relationship, e.g. linking polymeric viscosity to local shear-rate by using, for example, power-law models. A more physically sounded approach is to use a model relating the state of the microstructure in the solution with the macroscopic properties of interest. In this second approach, physically meaningful parameters are fitted using data from microscopic simulations or experiments. This approach can work well for simple flows (i.e., homogeneous deformation in a straightforward geometries) but problems often arise when applying the fitted model to more realistic flow processes.

Failure of the modeled constitutive equations to describe complex flows can be attributed to two different sources of error: 1) the microstructure variables do not follow the kinematics exactly (i.e., polymers chains conformation do not deform affinely) and/or 2) incorrect or insufficient physics are used to describe the microstructure effects on the macroscopic stress (i.e., polymer spring model etc.). Significant work has been dedicated to address the second source, and improve models performance through more complex physics. The Oldroyd,[3] the Finite Extensible Nonlinear Elastic with Peterlin closure (FENE-P),[4] the simplified Phan-Thien-Tanner sPTT,[5] and the Giesekus[6] models are only a few examples of constitutive models, each displaying distinct rheological behavior due to the different treatment of the polymeric entropy and the dynamics of the microstructure.

The time evolution of these constitutive equations can be split in reversible and irreversible parts. The reversible part is generally assumed to follow an Upper-Convected derivative, which comes from the natural idea that the polymers respond affinely to an applied deformation (i.e., velocity gradient). For the irreversible part, typically different constitutive closures (Oldroyd, FENE-P, Giesekus etc.) are used to model distinct non-Newtonian/viscoelastic responses. An alternative is to introduce complexity in the rheological behavior using a different choice for the time derivative (i.e., Lower-Convected or mixed derivative). For example, Oldroyd-A and Oldroyd-B models are originated from the same irreversible constitutive closure, albeit with two different choices of time derivative (i.e., Lower-Convected and Upper-Convected respectively). In particular, it can be useful to consider a mixed convected derivative that is balanced through an slip coefficient (i.e., Gordon-Schowalter type) when non-affine motion in the dynamics of polymeric solutions occurs. Gordon and Schowalter introduced an anisotropic fluid theory as an alternative to the Dumbbell theory that results in the well know Oldroyd-B model.[3,7] Non-affine motion is introduced as a

first order approximation to Ericksen theory[8] with an arbitrary constant (the slip coefficient) weighting the lower convected derivative contribution to the dynamics of the stress. The effect is referred to by different authors as slip,[7] non-affine motion,[9,10] and anisotropy or friction.[5,11] Somewhat surprisingly, a mixed derivative is seldom considered[12] although it has been shown to improve the performance of the extended Pom-Pom (XPP) and Phan-Thien-Tanner (PTT) models.[13] In fact, both non-affine deformation and internal microstructural response (mechanical elasticity-dissipation), can *independently* lead to non-Newtonian effects, and therefore they should be modelled *separately*. The difficulty to separate both sources of non-Newtonian behaviour has limited the number of studies addressing the possibility of non-affine motion of the chains.[13,14] However, it is still necessary to accurately calibrate the slip coefficient, and the constitutive closure equation appearing in these models independently to avoid mixing different sources non-Newtonian behavior.

In this work, we present a method to separate non-affine motion of chains from other sources of non-Newtonian behavior in dilute polymeric solutions. In our analysis, we assume that microstructure and rheological properties of a polymer solution system are well described with the local chain conformation tensor $\boldsymbol{c}$ given by

$$\boldsymbol{c} = \frac{1}{N_{\rm pol} q_0^2} \sum_i^{N_{\rm pol}} \boldsymbol{q}_i \boldsymbol{q}_i \tag{1}$$

where $N_{\rm pol}$ is the number of polymer molecules in a given domain and $\boldsymbol{q}_i$ is the end-to-end vector of each molecule in such a domain. The region including $N_{\rm pol}$ molecules should be small enough to allow for a continuum treatment but large enough to have a sufficiently large number of chains within. The resulting conformation tensor *field* couples with the mass and momentum balance equations leading to a complex rheology for the solution. Using the GENERIC framework, it has been shown that a general polymer model can be cast into the following set of partial differential equations governing flow[15]

$$\partial_t \rho = -\boldsymbol{\nabla}\cdot\rho\boldsymbol{v} \tag{2}$$

$$\partial_t \rho\boldsymbol{v} = -\boldsymbol{\nabla}\cdot\rho\boldsymbol{v}\boldsymbol{v} - \boldsymbol{\nabla}\cdot\boldsymbol{\Pi} + \eta_{\rm s}\nabla^2\boldsymbol{v} + \frac{\eta_{\rm s}}{3}\boldsymbol{\nabla}\boldsymbol{\nabla}\cdot\boldsymbol{v} + \rho\boldsymbol{g} \tag{3}$$

$$\partial_t \boldsymbol{c} = -\boldsymbol{v}\cdot\boldsymbol{\nabla}\boldsymbol{c} + \boldsymbol{c}\cdot\boldsymbol{\kappa} + \boldsymbol{\kappa}^T\cdot\boldsymbol{c} - \xi(\boldsymbol{c}\cdot\dot{\boldsymbol{\gamma}} + \dot{\boldsymbol{\gamma}}\cdot\boldsymbol{c}) + \frac{2}{\lambda_{\rm p} k_B T}\boldsymbol{c}\cdot\boldsymbol{\sigma} \tag{4}$$

The first equation is the continuity equation where, ρ is the mass density field and $\boldsymbol{v}$ is the velocity field. The second equation is the usual momentum balance equation in the form of the Navier-Stokes equation with solvent viscosity $\eta_{\rm s}$, but with a reversible stress given by $\boldsymbol{\Pi} = P\boldsymbol{I} + \boldsymbol{\sigma}\cdot\boldsymbol{c} + \boldsymbol{c}\cdot\boldsymbol{\sigma}$, where P is the pressure field of the solvent, $\boldsymbol{c}$ is the conformation tensor field, and $\boldsymbol{\sigma}$ is the conjugate variable of $\boldsymbol{c}$, given by the polymeric entropy $s_{\rm p}(\boldsymbol{c})$ of the fluid as:

$$\frac{\boldsymbol{\sigma}}{T} = \frac{\partial s_{\rm p}}{\partial \boldsymbol{c}} \tag{5}$$

Because the tensors $\boldsymbol{c}$ and $\boldsymbol{\sigma}$ commute,[15] the reminder of reversible stress can be expressed as $\boldsymbol{\tau} = 2\boldsymbol{c}\cdot\boldsymbol{\sigma}$ corresponding to the extra or polymeric stress. This additional contribution to the stress due to the microstructure results in the coupling of Eqns. (3) and (4). Equation (4) governs the evolution of the conformation tensor field $\boldsymbol{c}$. Its reversible part is given by the first three terms in the right hand side, determined by the flow kinematics. Here, $\boldsymbol{\kappa} = (\boldsymbol{\nabla}\boldsymbol{v})^T$ and $\dot{\boldsymbol{\gamma}} = (\boldsymbol{\kappa} + \boldsymbol{\kappa}^T)/2$. The fourth term in equation (4) describes slip or non-affine motion of the chain segments according to the Gordon-Schowalter (GS) equation,[7,16,17] where the slip coefficient $0 \leq \xi \leq 2$ quantifies the upper convected (UC) to lower convected (LC) contributions in the mix derivative. For example, for $\xi = 0$ the UC is recovered, $\xi = 2$ leads to a fully LC derivative, whereas $\xi = 1$ results in a corotational Jaumann-Maxwell derivative (See Appendix A 2). The slip term characterizes the non-affine motion in the continuum for the chains in solution or the network junctions in a melt.[7,9] This term is associated in the GENERIC framework with an antisymmetric friction matrix, this is, an irreversible contribution that, nevertheless, does not produce increase in the total entropy of the system.[17] The slip contribution can be understood as an overdamped version of a more detailed GENERIC theory with a fully symmetric friction matrix, in which a microscopic velocity near the suspended objects is an additional fast variable.[18,19] The slip contribution does not satisfy the Jacobi identity and, strictly speaking, cannot be considered as a mechanistic reversible contribution to the dynamics.[20,21] Nevertheless, for the sake of economy and on due account of being dissipation-less, we will refer to the first four terms in the right-hand side of (4) – including the slip term – as the reversible part of the dynamics.

We refer to the last term in Eqn. (4) – the polymeric entropy contribution – as the irreversible part of the conformation tensor dynamics. The intensity of this entropic term is determined by the polymeric relaxation time $\lambda_{\rm p}$. The structure of this irreversible part has been obtained in Ref.[15] under the assumption that the polymer solution is dilute, leading to a friction matrix (in GENERIC parlance) proportional to $\boldsymbol{c}$. Note however, that the last term in Eq. (4) can be generalized to more complex forms of the friction matrix, thus allowing the study of more concentrated systems and melts.[17]

II. WHY EVALUATE SLIP?

To justify the importance of the affine or non-affine character of the reversible dynamics of $\boldsymbol{c}$ (i.e., the need to include the slip term in Eq. (4)), it is useful to consider its effect on the dynamics of $\boldsymbol{c}$ using simplified models with known analytic expressions for the entropy s_p. This allows us to obtain solutions for the evolution of $\boldsymbol{c}$, the stress, and some important rheological properties with straight-forward interpretation. For a dilute solution of chains formed by Hookean dumbbells, we have Oldroyd-B model[3] whose entropy is given by[15,17],

$$s_{\rm p}^{\rm OB}(\boldsymbol{c}) = \frac{k_{\rm B}}{2}\left[\mathrm{tr}(\boldsymbol{I} - \boldsymbol{c}) + \ln(\det(\boldsymbol{c}))\right] \tag{6}$$

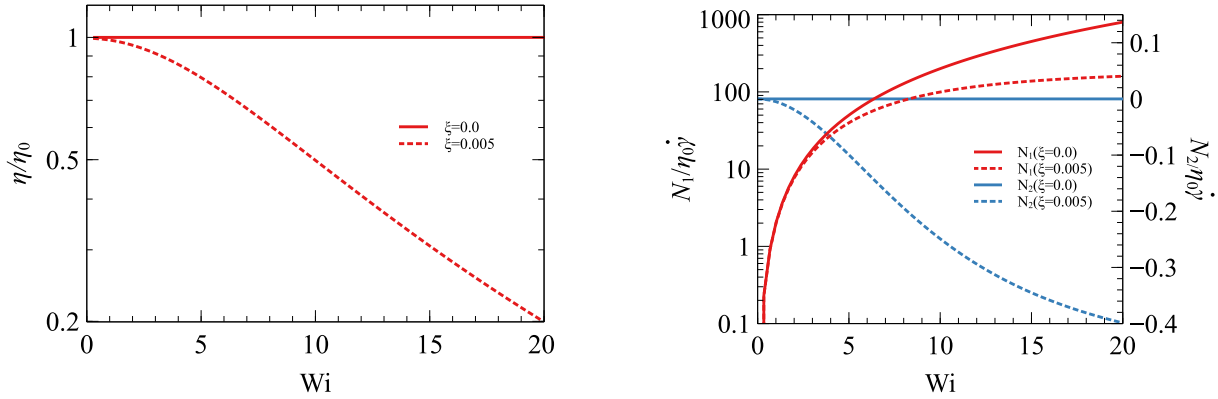

FIG. 1. Rheological behavior for "slipping" Oldroyd-B for affine $\xi = 0.0$ (solid lines) and non-affine $\xi = 0.005$ (dashed lines) simple shear flow results. **Left Panel:** Viscosity as a function of Wi. The inclusion of a small slip coefficient $\xi = 0.005$ results in dramatic shear thinning behavior. **Right Panel:** First and second normal stresses as a function of Wi. The first normal stress is reduced and a non-zero second normal stress appears with the inclusion of slip. The ratio of the two is given by the slip coefficient $N_2/N_1 = -\xi/2$.

For chains composed of FENE-P springs, we have the following expression for the polymeric entropy:[15,17]

$$s_{\rm p}^{\rm FENE}(\boldsymbol{c}) = \frac{k_{\rm B}}{2}\left[b\ln\phi(\boldsymbol{c}) + \ln\det\boldsymbol{c}\right] \tag{7}$$

where $\phi(\boldsymbol{c}) = \frac{b+D}{b} - \frac{1}{b}\mathrm{tr}(\boldsymbol{c})$ with D the dimensionality and b the finite extensibility parameter. Using Eqns. (5)-(7), the expressions for $\boldsymbol{\sigma}$ for both models are:

$$\boldsymbol{\sigma}^{\rm OB} = \frac{k_{\rm B}T}{2}(\boldsymbol{c}^{-1} - \boldsymbol{I}) \tag{8}$$

$$\boldsymbol{\sigma}^{\rm FENE} = \frac{k_{\rm B}T}{2}(\boldsymbol{c}^{-1} - \boldsymbol{I}/\phi(\boldsymbol{c})) \tag{9}$$

Using these two models we illustrate the importance of evaluating two possible sources of non-Newtonian behavior in polymer solutions: 1) slip or non-affine flow of chains, and 2) additional contributions to the polymeric entropy. First, we consider the Oldroyd-B model (OB) in Eq. (8) with slip $\xi \geq 0$ (but small) and refer to this more general model as "slipping" Oldroyd-B (SOB). In Figure 1, we show how including a small degree of non-affine motion results in a significant shear thinning in the shear viscosity η of the model fluid. Here, we have considered two contributions to the viscosity $\eta(\dot{\gamma}) = \eta_{\rm s} + \eta_{\rm p}(\dot{\gamma})$, where $\eta_{\rm p}$ is given by the polymeric contribution to the shear stress, which depends on the shear rate $\dot{\gamma}$. In Figure 1, we have normalized the viscosity by the zero shear viscosity $\eta_0 = \eta(\dot{\gamma}=0)$. As noted above, we considered $\xi = 0.005$ (i.e., a non-zero but small slip coefficient produces significant shear thinning without altering the entropic contribution to the evolution of $\boldsymbol{c}$ in Eq. (4)). In addition, the inclusion of slip results in an important reduction of the first normal stress N_1 and, most importantly, in a non-zero second normal stress N_2 in simple shear flow. Note that from these results we can confirm that $N_2/N_1 = -\xi/2$.[7] The ratio of the second and first normal stress is known as the "viscoelastic ratio" number, and relates elastic and viscous forces. This ratio has also been interpreted as representing the recoverable strain in the fluid.[22] The SOB model shows that non-Newtonian effects like shear thinning viscosity, or the presence of a second normal stress can be a direct result of non-affine motion of chains (4) (i.e., no additional physics are required to at least qualitatively describe this phenomena).

Next, we consider whether introducing slip is, in practice, equivalent to the application of more complex expressions for the polymeric entropy to account for non-Newtonian behavior. That is, if the rheological effect of non-affine deformation can be explained just as well by a different constitutive model for the polymer chains mechanical response. For this, we take the SOB model as our ground truth (i.e., treat it as experimental data), and then use FENE-P model in (9) without slip $\xi = 0$ as our to-be-fitted single parameter constitutive model. In Figure 2 , we adjust the FENE-P extensibility parameter $b = 50$ to fit a SOB($\xi = 0.05$) shear flow data (left panel). However, in the right panel, we show how using $b = 50$ the FENE-P model predictions fail to describe extensional rheology. Conversely, we could fit the extensional SOB data with the FENE-P model, but we will find a larger extensibility parameter b. Having different parameters in shear and extensional flows defeats the purpose of the constitutive modeling since most applied flows are a combination of shear and extension. Figure 2 exemplifies a common clash in the study of rheometric flows with models failing to simultaneously describe shear and extensional flows[23] or viscous (η) and elastic (N_1) effects with the same set of parameters.[24] This problematic lack of consistency is often addressed by matching the rheometric data with more complex models for the irreversible dynamics of the microstructure. For example, instead of including slip, we could generalize the Oldroyd-B model including a shear dependent viscosity.[25,26] If we apply this logic to our example, it is easy to see that the implemented modeling fix would not correspond with the physical reality – slip – and therefore, it is likely to misrepresent the rheology of the fluid (i.e., fail to describe extensional viscosity or normal stress). This top-down approach to model rheological behavior has been shown to lead to unphysical behavior. Introducing slip is in line with the alternative bottom-up approach, where model parameters depend on the microstructure of the fluid (i.e., the conformation tensor).[20,27]

An additional problem is the difficulty to disentangle non-Newtonian effects in the reversible and irreversible parts of the evolution equations for the microstructure. For example, measurable experimental quantities do not include the microstructure directly and therefore do not allow for the evaluation of non-affine motion. As we have shown, trying to explain all the features of the rheometric data through the irreversible part can lead to a lack of consistence like the one described above between shear and extensional rheology. In this study, we met the challenge of separating the reversible and irreversible parts in Eq. (4) with an elegant and efficient approach through an analysis of the eigenvalues and eigenvectors of $\boldsymbol{c}$. This allows us to establish whether or not slip is present in our microscopic simulations, and evaluate the validity of the upper convected derivative that is often taken for granted. More importantly, our approach provides a method to avoid mixing errors resulting from non-affine flow or slip in the reversible part, with the modeling errors in the irreversible part of the evolution equation. The ability to separate these two sources of error is a key step in the validation of constitutive models to ensure reliable predictions in different viscometric or complex mixed flows.

III. HOW TO EVALUATE SLIP?

The key step in evaluating non-affine motion is to look at the eigendynamics of the conformation tensor. We follow, Ref.[15] where we presented a discrete SPH model for a viscoelastic fluid, and described the dynamics of the conformation tensor in terms of its eigenvectors and eigenvalues. For completeness, we reproduce now the analysis for the case of the partial differential equation (4). We may write the conformation tensor dynamics (4) in the form

$$\frac{d}{dt}\boldsymbol{c} = \boldsymbol{c}\cdot\boldsymbol{\kappa} + \boldsymbol{\kappa}^T\cdot\boldsymbol{c} - \xi\,(\boldsymbol{c}\cdot\dot{\boldsymbol{\gamma}} + \dot{\boldsymbol{\gamma}}\cdot\boldsymbol{c}) + \frac{2}{\lambda_{\mathrm{p}} k_B T}\boldsymbol{c}\cdot\boldsymbol{\sigma} \tag{10}$$

where the substantial derivative is the first order differential operator

$$\frac{d}{dt} \equiv \frac{\partial}{\partial t} + \boldsymbol{v}\cdot\boldsymbol{\nabla} \tag{11}$$

We wish to express this evolution of the conformation tensor field in terms of its eigenvalues c_α, and orthonormal eigenvectors $\boldsymbol{u}_\alpha$ that satisfy

$$\boldsymbol{c}\cdot\boldsymbol{u}_\alpha = c_\alpha \boldsymbol{u}_\alpha \tag{12}$$

The conformation tensor field becomes

$$\boldsymbol{c} = \sum_\alpha c_\alpha \boldsymbol{u}_\alpha \boldsymbol{u}_\alpha^T \tag{13}$$

where the superscript T denotes transpose, so $\boldsymbol{u}_\alpha^T$ is a row vector.

The action of this linear differential operator on the spectral decomposition of the conformation tensor (13) is

$$\frac{d}{dt}\boldsymbol{c} = \sum_\gamma \frac{dc_\gamma}{dt}\boldsymbol{u}_\gamma\boldsymbol{u}_\gamma^T + \sum_\gamma c_\gamma \frac{d\boldsymbol{u}_\gamma}{dt}\boldsymbol{u}_\gamma^T + \sum_\gamma c_\gamma \boldsymbol{u}_\gamma \frac{d\boldsymbol{u}_\gamma^T}{dt} \tag{14}$$

Left and right multiplying both sides of (14) with the eigenvectors $\boldsymbol{u}_\alpha, \boldsymbol{u}_\beta$, respectively, we obtain

$$\boldsymbol{u}_\alpha^T\cdot\frac{d\boldsymbol{c}}{dt}\cdot\boldsymbol{u}_\beta = \frac{dc_\alpha}{dt}\delta_{\alpha\beta} + (c_\alpha - c_\beta)\frac{d\boldsymbol{u}_\alpha^T}{dt}\cdot\boldsymbol{u}_\beta \tag{15}$$

where we have used that $\frac{d\boldsymbol{u}_\alpha^T\cdot\boldsymbol{u}_\beta}{dt} = 0$ because the eigenvectors are orthogonal at all times. Left and right multiplying both sides of Eqn. (10) with the eigenvectors $\boldsymbol{u}_\alpha, \boldsymbol{u}_\beta$, and substituting (15) leads to

$$\boldsymbol{u}_\alpha^T\cdot\frac{d\boldsymbol{c}}{dt}\cdot\boldsymbol{u}_\beta = \left(1-\frac{\xi}{2}\right)c_\alpha\kappa_{\alpha\beta} + \left(1-\frac{\xi}{2}\right)c_\beta\kappa_{\beta\alpha} \tag{16}$$

$$-\frac{\xi}{2}c_\alpha\kappa_{\beta\alpha} - \frac{\xi}{2}c_\beta\kappa_{\alpha\beta} + \frac{2}{\lambda_{\mathrm{p}}N^p k_B T}\sigma_\alpha c_\alpha\delta_{\alpha\beta} \tag{17}$$

where we have introduced the matrix element of the velocity gradient tensor in the eigenbasis of the conformation tensor

$$\kappa_{\alpha\beta} \equiv \boldsymbol{u}_\alpha^T\cdot\boldsymbol{\kappa}\cdot\boldsymbol{u}_\beta \tag{18}$$

We have also introduced $\sigma_\alpha = \boldsymbol{u}_\alpha\cdot\boldsymbol{\sigma}\cdot\boldsymbol{u}_\alpha$ which are the eigenvalues of $\boldsymbol{\sigma}$. Note that both $\boldsymbol{\sigma}$ and $\boldsymbol{c}$ diagonalize in the same basis, i.e. they are coaxial tensors. One way to see this is by noting that they commute $\boldsymbol{\sigma}\cdot\boldsymbol{c} = \boldsymbol{c}\cdot\boldsymbol{\sigma}$, which is a necessary and sufficient condition for coaxiality.[15]

By equating Eq. (15) and Eq. (17), the diagonal and off-diagonal components lead to the following evolution equations for the eigenvalues and eigenvectors

$$\frac{dc_\alpha}{dt} = 2(1-\xi)c_\alpha\kappa_{\alpha\alpha} + \frac{2}{\lambda_{\mathrm{p}}N^p k_B T}c_\alpha\sigma_\alpha \tag{19}$$

$$\frac{d\boldsymbol{u}_\alpha}{dt} = \sum_\beta H^{\mathrm{mix}}_{\alpha\beta}\boldsymbol{u}_\beta \tag{20}$$

where the the antisymmetric matrix $H^{\mathrm{mix}}_{\alpha\beta}$ is given in its off-diagonal terms by

$$H^{\mathrm{mix}}_{\alpha\beta} = \frac{1}{c_\alpha - c_\beta}\left(1-\frac{\xi}{2}\right)(c_\alpha\kappa_{\alpha\beta} + c_\beta\kappa_{\beta\alpha}) - \frac{1}{c_\alpha - c_\beta}\frac{\xi}{2}(c_\alpha\kappa_{\beta\alpha} + c_\beta\kappa_{\alpha\beta}) \tag{21}$$

Note that Eq. (21) is not singular at equilibrium because the velocity gradient included in $\boldsymbol{\kappa}_{\alpha\beta}$ is zero. The partial differential Eqns. (19)-(21), together with the normalization of the eigenvectors $\mathbf{u}_\alpha$ are equivalent to the Eq. (4). However, they have the distinct feature of fully separating the reversible and irreversible dynamics of the conformation tensor. The evolution of the eigenvectors involve only the kinematics of the flow (i.e., what we are referring to as the reversible part of the dynamics), while all the irreversible behaviour, governed by the relaxation time λ_{p} appears in the eigenvalue equation. Any non-affine deformation of the chains leading to a non-vanishing slip coefficient $\xi > 0$ will therefore be reflected on the evolution of the eigenvectors $\boldsymbol{u}_\alpha$, which is independent of the irreversible dynamics considered by Eq. (19). Note that Eqns. (19)-(21) carry all the assumptions implicit in Eq. (4)

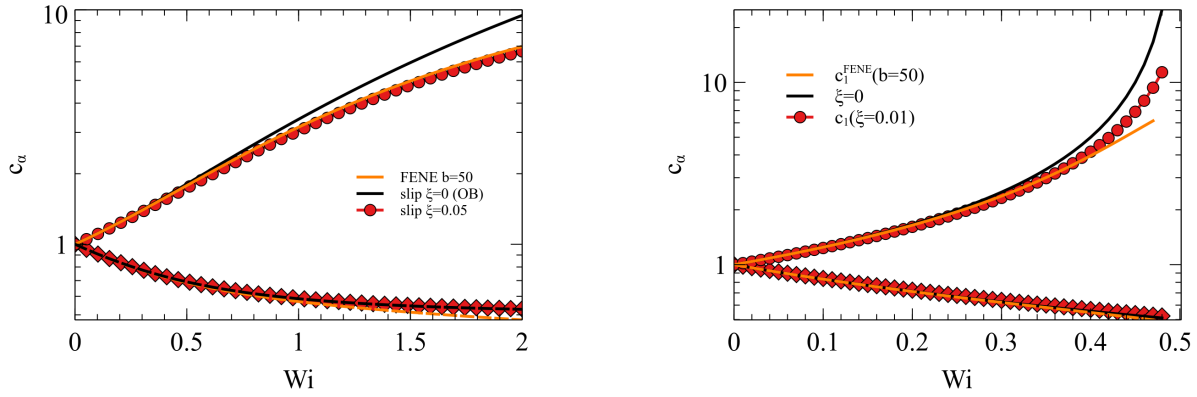

FIG. 2. **Left Panel:** Eigenvalues of the conformation tensor as a function of Wi in simple shear. **Right Panel:** Eigenvalues of the conformation tensor as a function of Wi in extensional flow. Red symbols represent the ground truth data (i.e., "slipping" OB model with $\xi = 0.05$). The black solid line corresponds with OB model or $\xi = 0.0$. The yellow solid lines correspond with the FENE-P model given by Eq. (9) and no slip. The finite extensibility parameter b can only be adjusted to describe shear or extensional flow but not both.

(i.e., are applicable to dilute systems). However, proposed approach can be applied to more general or complex versions of Eq. (4) that describe the rheology of concentrated solutions or entangled melts. For the separation of the reversible and irreversible parts to hold in the eigendynamics of the conformation tensor the only requirement is that $\boldsymbol{\sigma}$ and the friction matrix multiplying it in the last term of Eq. (4) remain functions of the eigenvalues of $\boldsymbol{c}$.

IV. COMPUTATIONAL DETAILS

The strategy that we follow in this work is to conduct microscopic simulations of a simple microscopic model for dilute polymer solutions with resolved monomer chains,[28] that it is taken as the "truth" behind a generic polymer solution. Using this model, previous detailed studies of the static properties and the rheological behavior of the solutions employed in the microscopic simulations have shown good agreement with theoretical predictions.[29,30] From the microscopic simulations, we will measure the macroscopic coarse-grained variables that appear in the macroscopic equations (2)-(4) in order to validate these equations. In particular, in this work we focus on the elucidation of the existence of non-affine motion described by a non-zero slip coefficient ξ. We study the non-affine character of the flow, which can be captured in the continuum equation (20).

A. Full monomer polymer solution

A semi dilute polymer solution is modelled at a detailed level with polymer molecules represented with a bead-spring model floating in a solvent. The solvent is modelled with the Smoothed Dissipative Particle Dynamics method (SDPD). SDPD presents a number of advantages over traditional Dissipative Particle Dynamics (DPD) and Smoothed Particle Hydrodynamics (SPH) methods: 1) it incorporates fluctuations in a particle-based Lagrangian discretization of Navier-Stokes (N-S) equations;[31] 2) it is compliant with the GENERIC formalism.[17] As a result, the method respects the First and Second Law s of Thermodynamics, and the incorporation of thermal fluctuations leads to the correct equilibrium probability distribution given by Einstein's formula.[31] In addition, 3) SDPD model parameters are directly connected to the physical parameters (density, speed of sound, and viscosity) of the simulated system making it possible to give a physical interpretation of the simulation results.[32] In SDPD, the fluctuating N-S equations are discretized to a set of stochastic differential equations for the position $\boldsymbol{r}_i$, velocity $\boldsymbol{v}_i$ and entropy S_i of a set of discrete N_{SDPD} particles.[31] In the present work, we consider only the mass and momentum balances since we are working with isothermal flows. The evolution of the particles position and momentum are given by

$$\frac{d\boldsymbol{r}_i}{dt} = \boldsymbol{v}_i \tag{22}$$

$$m\frac{d\boldsymbol{v}_i}{dt} = \boldsymbol{F}_i \tag{23}$$

where $\boldsymbol{F}_i$ is the force acting on each SDPD particle that can be split on its conservative (c), dissipative (d), random (r) and external (e) contributions (i.e., $\boldsymbol{F}_i = \sum_j \left(\boldsymbol{F}^{\text{c}}_{ij} + \boldsymbol{F}^{\text{d}}_{ij} + \boldsymbol{F}^{\text{r}}_{ij}\right) + \boldsymbol{F}^{\text{e}}_i$). Note that all force contributions with the exception of the external force result from the sum of pair interaction among fluid particles. Each contribution is given by

$$\boldsymbol{F}^{\text{c}}_{ij} = -\sum_j \left[\frac{p_i}{d_i^2} + \frac{p_j}{d_j^2}\right] \tilde{F}_{ij}\boldsymbol{r}_{ij} \tag{24}$$

$$\boldsymbol{F}^{\text{d}}_{ij} = -\sum_j \left[a_{ij}\boldsymbol{v}_{ij} + b_{ij}(\boldsymbol{v}_{ij}\cdot\boldsymbol{e}_{ij})\boldsymbol{e}_{ij}\right] \frac{\tilde{F}_{ij}}{d_i d_j} \tag{25}$$

$$\boldsymbol{F}^{\text{r}}_{ij} = \sum_j \left[A_{ij}d\overline{\boldsymbol{W}}_{ij} + \frac{B_{ij}}{3}\text{tr}(d\boldsymbol{W}_{ij})\right]\cdot\boldsymbol{e}_{ij} \tag{26}$$

where $\boldsymbol{r}_{ij} = \boldsymbol{r}_i - \boldsymbol{r}_j$, $\boldsymbol{v}_{ij} = \boldsymbol{v}_i - \boldsymbol{v}_j$ and $\boldsymbol{e}_{ij} = \boldsymbol{r}_{ij}/r_{ij}$. The particle density is calculated as $d_i = 1/\mathscr{V}_i = \sum_j W_{ij}$, where

$W_{ij} = W(r_{ij}, r_c)$ is a normalized kernel function of finite support r_c. The gradient of the weight function provides the function $\tilde{F}_{ij} = -\nabla W(r_{ij}, r_c)/r_{ij}$. Following previous work using SDPD particles we have adopted Lucy kernel:[33]

$$W(r, r_c) = \begin{cases} \frac{105}{16\pi r_c^3}\left(1+3\frac{r}{r_c}\right)\left(1-\frac{r}{r_c}\right)^3 & \text{if } r/r_c \le 1 \\ 0 & \text{if } r/r_c > 1 \end{cases} \quad (27)$$

In Eq. (24) above the pressure p_i is given by Tait's equation of state:[34]

$$p_i = p_0\left[\left(\frac{\rho_i}{\rho_0}\right)^{\gamma} - 1 + \varepsilon\right] \quad (28)$$

where p_0, ρ_0 and γ parameters are chosen to minimize density variations ($< 5\%$) by choosing a sufficiently large speed of sound $c_s = \sqrt{p_0\gamma/\rho_0}$. A background dimensionless pressure contribution $\varepsilon = 0.7$ ensures positive pressure across the domain for the range of deformation rates studied, which provides numerical stability.[33] In Eq. (25), $a_{ij} = 5\eta/3 - \zeta$ and $b_{ij} = 5(\zeta + \eta/3)$ are friction coefficients given by the shear η and bulk ζ viscosities. In Eq. (26), the amplitudes of the thermal noises A_{ij} and B_{ij} are chosen to satisfy the Fluctuation-Dissipation Theorem:

$$A_{ij} = \left[4k_B T a_{ij}\frac{\tilde{F}_{ij}}{d_i d_j}\right]^{1/2} \quad (29)$$

$$B_{ij} = \left[4k_B T\,(b_{ij} - a_{ij}/3)\,\frac{\tilde{F}_{ij}}{d_i d_j}\right]^{1/2} \quad (30)$$

For the random contribution to the force in Eq. (26), $d\boldsymbol{W}_{ij}$ is a matrix of independent increments of the Wiener process and $d\overline{\boldsymbol{W}}_{ij}$ its traceless symmetric part. For additional details on the SDPD model and its implementation the reader is referred to previous work.[31,32]

The polymer chains are modelled by linking solvent-like particles with Finite Extensible Non-linear Elastic (FENE) springs:[35]

$$\boldsymbol{F}_{ij}^{\text{FENE}} = \frac{H\boldsymbol{r}_{ij}}{1 - (r_{ij}/r_{\max})^2} \quad (31)$$

where $H = bk_BT/r_{\max}^2$ is the spring elastic constant, $\boldsymbol{r}_{ij}$ is vector connecting two consecutive particles forming a polymer chain, $r_{\max} = 1.4dx$ is the limit value for the extensibility of the spring and b a scale factor balancing elastic and thermal forces acting on the particles. Note that polymer topology is preserved thanks to the choice of a small maximum bond length relative to the average inter-particle distance $dx = 1$ (i.e., bond crossing is prevented). Under these conditions the system quickly equilibrates to a bond length $l \sim 0.6dx$ which is roughly 40% of the limit extensibility. The equilibrium value of l is not strongly affected by the flow conditions in the study. This method for generating chains of SDPD particles have been shown to reproduce the right scaling for static properties and diffusion coefficient of single polymer chains.[29] For solutions constructed in this way with N_{pol} polymer chains of N_{mon} monomers each we define the effective polymer concentration

$$w = \frac{N_{\text{mon}}N_{\text{pol}}}{N_{\text{SDPD}}} \quad (32)$$

where N_{mon} is the number of monomers per chain, N_{pol} is the number of polymer chains, and N_{SDPD} is the total number of solvent fluid SDPD particles in the simulation. Note that given that the SDPD viscous interactions between all particles (polymer or solvent) are always active, a concentration of $w = 1$ is still representative of a polymer solution.[29,30,36] A summary of the parameters for the SDPD particles and spring constants solutions is included in Table I. We have chosen a set of unit-less parameters that determine the dimensionless numbers characterizing the flow that are compatible with experiments Reynolds $0.1 - 10$, Weissenberg $0.1 - 100$ and Schmidt ~ 1000.[30] However, an appropriate selection of dimensional base parameters (i.e., maximum extensibility $r_{\max}$, mass density ρ and dynamic viscosity η) will yield the equivalent parameter space in SI units.[37]

TABLE I. Model parameters for the microscopic SDPD simulations.

Parameter	Description	Value
dx	average inter-particle distance	1.0
Δt	simulation timestep	0.003
ρ	density	1.0
m	particle mass	1.0
w	chain concentration	0.1
η_s	solvent viscosity	5.0
c_s	speed of sound	10
ε	background pressure	0.7
h	smoothing length	$3dx$
k_BT	thermal energy	1.0
b	FENE-P spring constant	100
$r_{\max}$	max. extensibility radius	$1.4dx$

B. SPH discretization of continuum equations, coarse-graining and mapping

The objective is to use microscale data from the full monomer polymer solution simulations in order to check if the macroscale Eq. (20) is satisfied for ξ=0. Otherwise, we employ Eqns. (20) and (21) to measure the slip parameter ξ. This requires to discretize the continuum field equations, and define a mapping from the microscopic simulation data to the discrete macroscopic variables. In this paper, we focus on shear flows, for which the system is traslationally-invariant along the direction normal to the flow. Therefore, and for the sake of compiling sufficient statistics, the discretization takes place on a 2D Eulerian grid with N_{latt} nodes at the square lattice positions $\boldsymbol{R}_\mu \in \mathbb{R}^2, \mu = 1, \cdots, N_{\text{latt}}$, as shown in the right panel of Fig. 3. As we consider pure shear flow, where the flow is invariant in the direction of the velocity field, the term

$\boldsymbol{v}\cdot\boldsymbol{\nabla}\boldsymbol{u}_\alpha$ in the substantial derivative vanishes, and we have

$$\frac{\partial \boldsymbol{u}_\alpha}{\partial t} = \sum_\beta H^{\rm mix}_{\alpha\beta}\boldsymbol{u}_\beta \tag{33}$$

This equation is a partial differential equation involving the fields $\boldsymbol{v}, \mathbf{u}_\alpha, c_\alpha, \boldsymbol{\kappa}$. Note that, the velocity gradient $\boldsymbol{\kappa}$ appears within $H^{\rm mix}_{\alpha\beta}$, as shown in (18) and (21). Equation (33) can be discretized in a number of ways (finite differences, elements, etc.). We choose here an SPH discretization $[\boldsymbol{v}]_\mu, [\boldsymbol{u}_\alpha]_\mu, [c_\alpha]_\mu, [\boldsymbol{\kappa}]_\mu$ with a weight function that is the same as the one we use to define the CG variables inferred from the microscale simulation in subsection IV A. For example, the velocity at the μ-th node is given by

$$[\mathbf{v}]_\mu = \frac{\sum_i \mathbf{v}_i W_{i\mu}}{\sum_i W_{i\mu}} \tag{34}$$

where we use Latin indices for microscopic variables and Greek indices for macroscopic ones. The notation $[\cdots]_\mu$ denotes the quantity associated to node μ in the square lattice. The denominator corresponds to the "particle density" evaluated at the cell location given by

$$d_\mu = \sum_i W_{i\mu}. \tag{35}$$

The SPH method gives the following ordinary differential equations for (33)

$$\frac{d[\boldsymbol{u}_\alpha]_\mu}{dt} = \sum_\beta \left[H^{\rm mix}_{\alpha\beta}\right]_\mu \left[\boldsymbol{u}_\beta\right]_\mu \tag{36}$$

where

$$\begin{aligned}&\left[H^{\rm mix}_{\alpha\beta}\right]_\mu \\ &= \frac{1}{[c_\alpha]_\mu - [c_\beta]_\mu}\left(1-\frac{\xi}{2}\right)\left([c_\alpha]_\mu[\kappa_{\alpha\beta}]_\mu + [c_\beta]_\mu[\kappa_{\beta\alpha}]_\mu\right) \\ &- \frac{1}{[c_\alpha]_\mu - [c_\beta]_\mu}\frac{\xi}{2}\left([c_\alpha]_\mu[\kappa_{\beta\alpha}]_\mu + [c_\beta]_\mu[\kappa_{\alpha\beta}]_\mu\right)\end{aligned} \tag{37}$$

The term $[\kappa_{\beta\alpha}]_\mu$ involves space derivatives, which are computed in the SPH discretization according to[31]

$$\begin{aligned}[\kappa_{\beta\alpha}]_\mu &= [\mathbf{u}_\alpha]_\mu \cdot [\boldsymbol{\nabla}\boldsymbol{v}]_\mu \cdot [\mathbf{u}_\alpha]_\mu \\ [\boldsymbol{\nabla}\boldsymbol{v}]_\mu &= \frac{\sum_i W'_{i\mu}\boldsymbol{e}_{i\mu}\left([\boldsymbol{v}]_\mu - [\boldsymbol{v}]_i\right)}{\sum_i W_{i\mu}}\end{aligned} \tag{38}$$

where the prime denotes the derivative with respect to r (i.e., $W'_{i\mu} = \frac{\partial W}{\partial r}|_{r=r_{i\mu}}$).

The conformation tensor of node μ is defined microscopically as

$$[\boldsymbol{c}]_\mu = \frac{1}{q^2_{\rm eq}}\frac{\sum_{a=1}^{N_{\rm pol}} \mathbf{q}_a\mathbf{q}_a W^*_{a\mu}}{\sum_{a=1}^{N_{\rm pol}} W^*_{a\mu}} \tag{39}$$

where $\boldsymbol{q}_a = \boldsymbol{r}_N - \boldsymbol{r}_1$ is the end-to-end vector of the a-th polymer chain which has an averaged equilibrium length $q_{\rm eq}$. In this case, $W^*_{a\mu} = W(\|\boldsymbol{R}_\mu - \boldsymbol{X}^{\rm cm}_a\|, r_{\rm c})$, with $\boldsymbol{X}^{\rm cm}_a$ being the center of mass of the a-th chain. The sum runs over the $N_{\rm pol}$ polymer molecules in the system, and $W^*_{a\mu}$ is the weight function evaluated at the distance between the center of mass of the a-th polymer and the node μ. Therefore, the conformation tensor $[\boldsymbol{c}]_\mu$ contains contributions of polymer molecules that are around node μ. The velocity of the nodes $[\boldsymbol{v}]_\mu$ is a 3-component vector, and the velocity gradient $[\boldsymbol{\nabla}\boldsymbol{v}]_\mu$ and conformation tensors $[\boldsymbol{c}]_\mu$ are represented by a 3×3 matrices that live in a 2D space, that of the square lattice (See Figure 3).

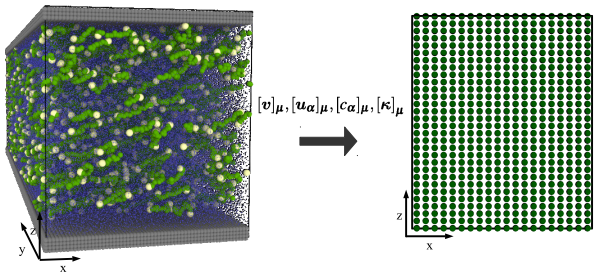

FIG. 3. The 3D mesoscopic system on the left ($60\times100\times66$), is coarse-grained to produce the values of the velocity gradient and conformation tensors at each of the 20×22 nodes of the grid on the right. On the mesoscopic 3D system, with relative concentration $w = 0.1$, the size of the solvent particles (blue) has been reduced to facilitate the visualization of the chains (green), chain ends (yellow) and wall particles (grey).

A word about the argument of the kernels appearing in (34)-(39) is in order. These kernels depend on the distance between the position $\mathbf{r}_i \in \mathbb{R}^3$ and the lattice positions $\mathbf{R}_\mu \in \mathbb{R}^2$. They are computed by stripping off the component in the neutral direction of the position $\mathbf{r}_i$, in such a way that then it becomes a vector $\mathbf{r}^*_i \in \mathbb{R}^2$. Then the substraction of $\mathbf{r}^*_i$ and $\mathbf{R}_\mu$ is a bona fide mathematical operations that allows to compute the distance. This is equivalent to understand the nodes as "cylinders" in the neutral direction. For additional details see Appendix A 1.

Substitution of (37), (38) into (36) renders the continuum Eqn. (33) into an ordinary differential equation involving the node variables $[\boldsymbol{v}]_\mu, [\boldsymbol{u}_\alpha]_\mu, [c_\alpha]_\mu, [\boldsymbol{\kappa}]_\mu$. Direct numerical evaluation of Eq. (36) presents some problems due to the need of differentiating the evolution of $\boldsymbol{u}_\alpha$ in time, which is error prone. However, Eq. (36) can be rewritten explicitly in integral form for each eigenvector $\boldsymbol{u}_\alpha$. For the first eigenvector $\boldsymbol{u}_1$, we have

$$u^x_1(t) - u^x_1(t_0) = \int_{t_0}^t (H^{\rm mix}_{12}u^x_2 + H^{\rm mix}_{13}u^x_3)dt' \tag{40}$$

$$u^y_1(t) - u^y_1(t_0) = \int_{t_0}^t (H^{\rm mix}_{12}u^y_2 + H^{\rm mix}_{13}u^y_3)dt' \tag{41}$$

$$u^z_1(t) - u^z_1(t_0) = \int_{t_0}^t (H^{\rm mix}_{12}u^z_2 + H^{\rm mix}_{13}u^z_3)dt' \tag{42}$$

where the superscripts indicate coordinate components (x,y,z). Equivalent expressions can be written for the eigenvectors $\boldsymbol{u}_2$ and $\boldsymbol{u}_3$. Since these evolution equations reflect the

reversible part of the dynamics, they will provide complete information on the specific convective character of the derivative of **c** in a macroscopic model.

V. RESULTS

In this section, we first characterize the rheology of the model polymeric solutions with chains lengths N=10 and N=20, and concentrations w ranging from 0.05 to 1 using Reverse Poiseuille Flow simulations. Then, we introduce our Couette flow simulations for the analysis of the effect of slip in simple shear. Finally, we apply the microscopic to macroscopic mapping procedure described above to determine the magnitude of the slip coefficient in our model fluids.

A. Reverse Poiseuille flow simulations

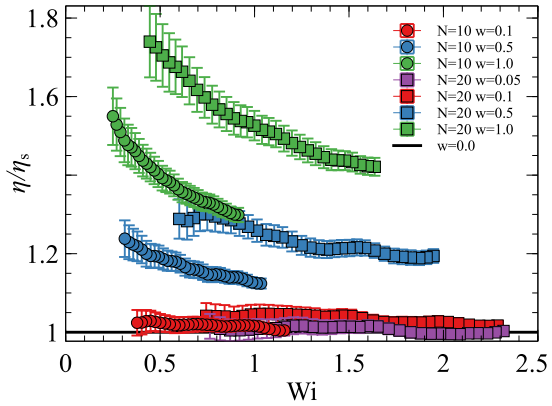

FIG. 4. Shear viscosity of N=10 and N=20 solutions as a function of the Weissenberg number for different polymer concentration (indicated by the legend). The black line shows the solvent viscosity $\eta_s = 5$.

We characterize the viscoelastic response of the solutions by using Reverse Poiseuille Flow (RPF), which consist of two parallel Poiseuille flows in opposing directions driven by uniform body forces.[36] This method has the singular advantage of avoiding the need of fixed walls, where boundary conditions like no slip need to be imposed.[38] The flow is simply imposed by dividing the simulation domain in two halves and applying a uniform external force in the x-direction $\boldsymbol{F}^e = (F_x^e, 0, 0)$. In the first half of the domain $F_x^e = g$ and in the second half $F_x^e = -g$. Additional details on the implementation of the method are given elsewhere.[30] Figure 4 presents the viscosity (i.e., $\eta = \tau_{xy}/\dot{\gamma}$) normalized by the solvent viscosity η_s as a function of the Weissenberg number Wi=$\dot{\gamma}\lambda_p$ in solutions for chains N=10 and N=20, and with chain concentrations w =0.05, 0.1, 0.5 and 1.0. The viscosities are calculated once steady-state flow of is reached. The viscosity profiles presented in Figure (4) are the result of further averaging the stress in time (i.e., an averages of every 1000 time steps for each bin is given with a timestep $\Delta t = 0.003$). The timestep for all our simulations is given by the shorter time scale in the Courant-Friedrich-Lewy condition $\delta t_c = dx/32c_s$ and $\delta t_\eta = dx^2/16\eta$.[39,40] A characterization of the polymeric relaxation time λ_p as a function for the chain length and concentration in the model fluids is discussed in ref.[30]. Here, we consider $\lambda_p(N = 10) = 5$ and $\lambda_p(N = 20) = 10$ for a range concentrations w =0.05 to 1 as defined by Eq. (32).

B. Slip in Couette flow simulations

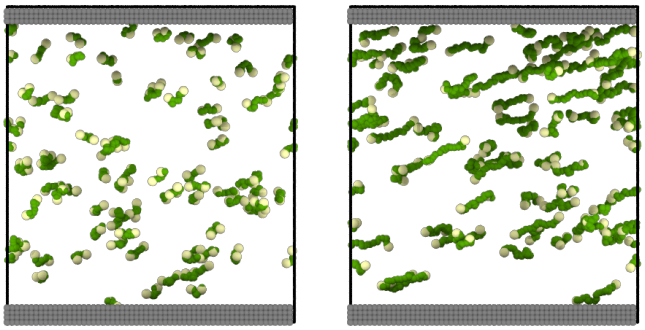

FIG. 5. xz-plane view of the 3D simulation domain. Wall particles in grey, backbone chain particles in green and chain ends in light yellow. Only a limited selection of chains is displayed to facilitate visualization of the stretching and orientation in flow. The solvent particles and the rest of the chains have been hidden. The images correspond to steady-state flow at Wi=11 at a concentration $w = 0.1$. Top wall moves forward and bottom wall moves backwards. **Left Panel:** Chain length N=10. **Right Panel:** Chain length N=20.

For the microscopic simulations, we employ a simulation cell of dimensions (60x100x66) where two walls of regularly spaced particles (dx=1) with a wall thickness of $3dx$ are introduced in the z-direction in the regions $0 \leq z \leq 3$ and $63 \leq z \leq 66$ (See Figure 5). This gives a fluid domain with a vertical dimension of $L_z = 60$.

To avoid confinement effects we limit our simulations to relatively short chains of length $N = 10$ and $N = 20$ with an equilibrium radius of gyration $R_g \sim 1.3$ and ~ 1.8 which is roughly $1/50$ and $1/30$ the gap between the moving walls, respectively. Therefore, the distance between the walls is much larger than the characteristic coil size. In the evaluation of the integrals in Eqns. (40)-(42) we have eliminated the layers closest to the channels walls (i.e., excluding $3dx \sim R_g$) from our analysis since the close proximity to the walls affects the conformation of the chains.[30]

In our analysis, the domain is divided into bins shaped as layers piling up in the vertical z direction. Due to the shear flow conditions, the velocity $[\boldsymbol{v}]_\mu$ and conformation tensor $[\boldsymbol{c}]_\mu$ are homogeneous within each bin and are, for the sake of good statistics, averaged over the nodes in the same bin.

The microscopic simulations are run during an equilibration time after which the polymer chains are randomly distributed and oriented. From this initial configuration, a start-up flow is imposed by displacing the upper and lower walls

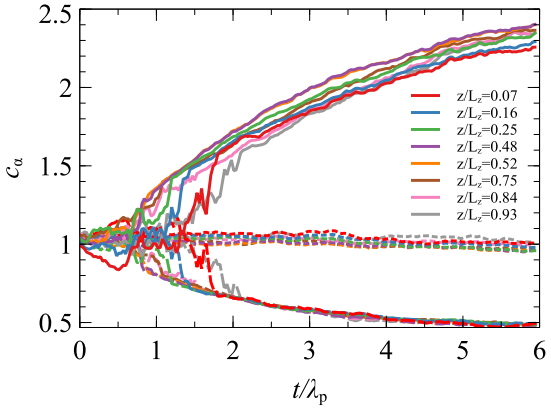

FIG. 6. Eigenvalues of the conformation tensor at different height bins in the $z-$direction. c_1 and c_3 are represented by solid and dashed lines respectively. The neutral direction c_2, which remains unaltered by flow, is shown by doted lines. The color coding indicates the normalized coordinate z/L_z.

in the x-direction with velocities v_{wall} and $-v_{\text{wall}}$ respectively. To avoid an additional time-scale given by systems' inertia, at time $t=0$ we impose to all particles in the fluid a linear velocity profile given by the walls velocity. This results into a linear velocity profile with a constant shear rate $\dot{\gamma}=2v_{\text{wall}}/L_z$. Although, a linear velocity profile is only imposed at t=0, no significant variation to the velocity profile is observed throughout the transient Couette flow simulations. As a result of the imposed shear flow the chains in the fluid domain get first oriented and then stretched, as shown in Fig. 5. The stretching and orientation of the chains is reflected macroscopically in the behaviour of the eigenvalues and eigenvectors of the conformation tensor, that evolve homogeneously through the start-up shear flow simulations.

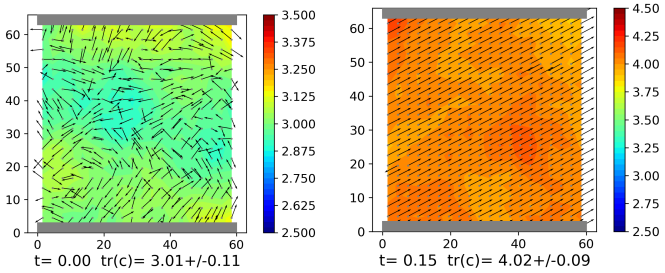

FIG. 7. xz-plane view of the simulation domain with the first eigenvectors $\boldsymbol{u}_1$ marked by black arrows at each lattice position. The coloring follows the trace of the conformation tensor $\boldsymbol{c}$ which, at equilibrium, takes the value $\text{tr}[\mathbf{c}]=3$ and at steady-state flow reaches roughly a value of 4 for this example with chains N=10. **Left Panel:** Initial equilibrium configuration. **Right Panel:** Final configuration.

After mapping the conformation tensor $\mathbf{c}$ on the coarse-grained grid, we diagonalize it and monitor the resulting eigenvalues/vectors dynamics. In Fig. 6 we show the eigenvalues of the mapped $[\mathbf{c}]_\mu$ as a function of time during the start-up shear flow. Here, we have considered layers of the macroscopic lattice points and averaged the values in the x-direction. The corresponding layer height in the z-direction is displayed in the legend of Fig. 6. We observe an increase of the first eigenvalue c_1, and a decrease of the third eigenvalue c_3, while the second eigenvalue c_2 remains constant as it corresponds to the neutral direction in Couette flow. This behaviour is consistent with an alignment of the conformation tensor ellipsoid in the $xz-$plane. At the end of the simulations with a duration of approximately six times the polymeric relaxation time λ_p, we observe how the eigenvalues of the conformation tensor $\boldsymbol{c}$ plateau towards the steady-state values. In Fig. 6, we notice that the two layers closer to the walls $z/L_z=0.07$ and $z/L_z=0.93$ show a delay on their stretching and slightly lower stretching at the end of the simulation, with respect to the other layers inside the fluid domain. We attribute this behavior to a combination of exclusion and interaction with the walls.[30] In the remainder of our analysis we will consider only the layers containing chains whose center of mass is located between $0.16\leq z/L_z\leq 0.84$ (i.e., effectively the first and last lattice layers of the macroscopic lattice are excluded from our analysis).

Two snapshots of the eigenvector $\boldsymbol{u}_1$ field corresponding to initial equilibrium and final states of the start-up shear flow are shown in Fig. 7. The coloring in Fig. 7 follows the trace of the conformation tensor $\text{tr}(\boldsymbol{c})=c_1+c_2+c_3$. Initially the eigenvectors are randomly distributed and overall the trace $\text{tr}(\boldsymbol{c})\simeq 3$. This is also observed in Figure 6, where initially the eigenvalues of $\boldsymbol{c}$ are all unity within the statistical error. At the end of the start-up flow simulations, that extend to roughly six relaxation times, clear alignment is seen in the final state, and little to no variation in the eigenvalues and eigenvectors is observed. Given the initial random distribution for the direction of the eigenvectors, the integrals in Eqns. (40)-(42) are evaluated from some time $t_0>0$ during transient flow. Note that Eqns. (40)-(42) must be evaluated in transient flow since once steady-state is reached they are trivially satisfied. The left hand side goes to zero because the orientation of the eigenvectors is fixed, as seen in the right panel of Fig. 7. The right hand side also goes to zero as $\boldsymbol{\kappa}_{\alpha\beta}$ goes to zero due to the alignment of $\boldsymbol{\kappa}$ with the eigenvectors $\boldsymbol{u}_\alpha$.

In order to check the presence of slip in the dynamics of eigenvectors that are governed by Eqns. (40)-(42), we plot the right hand side of these equations as a function of the left hand side. In these plots, a slope of one indicates that Eqns. (40)-(42) are satisfied. Note that in the neutral y-direction Eq. (41) is trivially satisfied for this specific flow geometry. In Fig. 8, we evaluate the presence of slip for a solution of chains of size $N=10$ and at a concentration $w=0.1$, using different values of the slip parameter ξ=0.0, 0.02 and 0.1 in Eq. (21). Here, we have also considered the average in the x-direction at layers of the macroscopic lattice of points distributed along the z-direction (i.e., left and right hand sides of Eqns. (40)-(42) evaluated as averages in the x-direction). The best agreement between the left- and right-hand side of Eqns. (40)-(42) is achieved for ξ=0. In addition, we find that as we discussed in the previous section for the eigenvalues of $\boldsymbol{c}$, the evolution of the eigenvectors in Fig. 8 is homogeneous in the z-direction during the transient flow, if one excludes the layers closest to

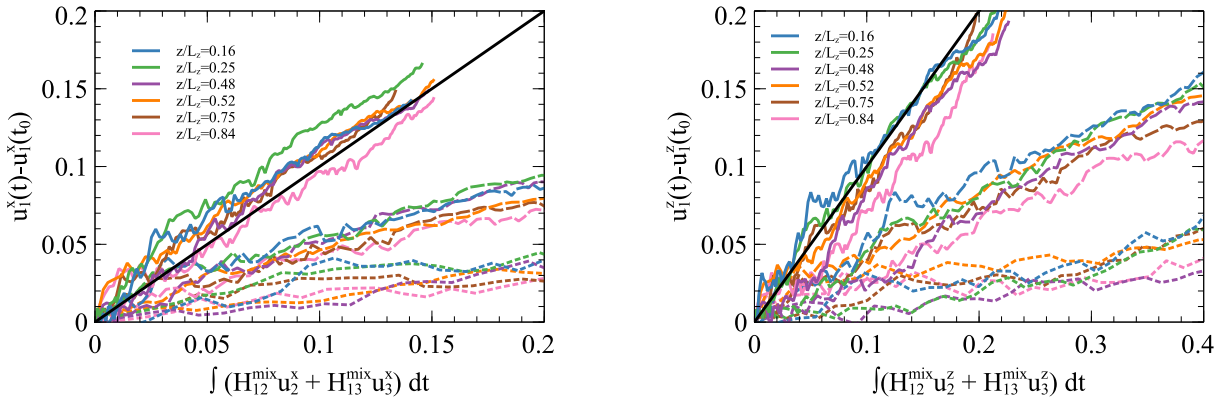

FIG. 8. **Left Panel:** The right hand side of Eq. (40) as a function of its left hand side, for N=10 and w=0.1, for the different bins. Three values of $\xi = 0.0$ (solid lines), $\xi = 0.02$ (dashed lines), $\xi = 0.1$ (dotted lines) are shown. **Right Panel:** Equivalent evaluation of the z-component of the first eigenvector given by Eq. (42).

the solid walls. We conclude that a more clear picture of the effect of slip in our analysis can be achieved by also averaging in the z-direction through the height of the channel (i.e., averaging over the simulation domain but excluding the layers closest to the walls). The average of the curves in Fig. 8 is shown in Fig. 9. The best agreement (i.e., a slope of one), between the left and right hand sides of Eqns. (40) and (42) is now more clearly seen for $\xi = 0.0$. Therefore, we can conclude that, for this system with N=10 and w=0.1, the chains are deforming affinely with the flow. We note that this case corresponds with the smallest chains at the lowest concentration in our study, where inter-chain interaction effects are expected to be negligible.

To continue our analysis, we first consider higher concentrations with chains of length N=10. Using the fully averaged representation in the x- and z-directions, we observe that the flow ceases to be affine as we increase the concentration (See Fig. 10). For concentrations w=0.5 and w=1.0 in Fig. 10 center and right panels, we find that Eq. (40) is satisfied for ξ=0.005. This result suggests that the slip coefficient plateaus for concentrations $w \gtrsim 0.5$ in solutions with chains N=10. We note that the same dependence of the slip coefficient ξ is obtained when comparing the $z-$component of the eigenvectors in Eq. (42).

Next, we considered a set of simulations with chains that are twice as long (N=20) as in the previous examples. We find a continuously increasing trend with slip parameter ξ=0.0035, 0.005, 0.007 and 0.008 for concentrations w=0.05, 0.1, 0.5 and 1.0. Figure 11 shows the evaluation of Eq. (40), where the increasing trend for the slip coefficient for the first three concentrations in the systems with chain length N=20. For these systems, a plateauing is also observed for higher concentrations. The slip coefficient becomes smaller at low concentrations, but the concentration at which the slip coefficient is negligible is not reached. Note that the study of concentrations lower than w=0.05 is limited by the simulation size required to achieve statistical significance. However, given the decreasing trend, one should expect that the slip coefficient will go to zero at small enough concentrations. As in the case of N=10 solutions, for N=20 the same results for the slip coefficient as a function of the concentration is found for the evaluation of the z-component of the eigenvector through Eq. (42).

The increase in the slip coefficient ξ with chain length N and concentration w indicates that the non-affine evolution of the conformation tensor eigenvectors is related to the inter-chain contacts and/or interactions in the solution. We observe that the larger the chain coil size the lower is the concentration required to produce slip with respect to the imposed flow. In addition, the fact that the same slip parameters are obtained simultaneously for both x- and z-components of the eigenvectors gives a strong support to the physical origin of slip, and to the validity of the form in Eq. (4) introducing slip through the Gordon-Schowalter derivative.

Finally, we summarize the observed trends in the slip coefficient with chain length and concentration in Fig. 12. As shown by our simulation results in Figures 8-11, the slip coefficient ξ increases with both chain length and concentration in Figure 12. For the lower concentrations, the slip coefficient decreases, and becomes zero for N=10 and w=0.1. On the other hand, a clear plateau is observed at higher concentrations, where for concentrations $w \gtrsim 0.5$ further increasing w has little to no effect on ξ for either chain length. These trends make physical sense since both chain length and concentration will increase the interactions between chains and, therefore, reduce the mobility of chain segments. The reduced mobility can be understood as a resistance for the chains to orient that results on the non-affine motion of chains. We note that the slip coefficients that we find in this study are very small, with the highest ξ=0.008 found for chains N=20 and w=1.0. This indicates that only small fraction of the mix derivative in Eq. (4) is given by the contribution of a lower convected derivative. Experimental studies have reported the ratio $-N_2/N_1$ to be in the range 0.05-0.3, which will suggest a much larger slip coefficient.[13] Nevertheless, as we have discussed in Sec. II, even small values of the slip coefficient may affect significantly the rheology of the solution. Furthermore, the determination of the slip coefficient ξ through the ratio $-N_2/N_1$ does not separate the sources of non-Newtonian and viscoelastic behavior arising from the reversible and irre-

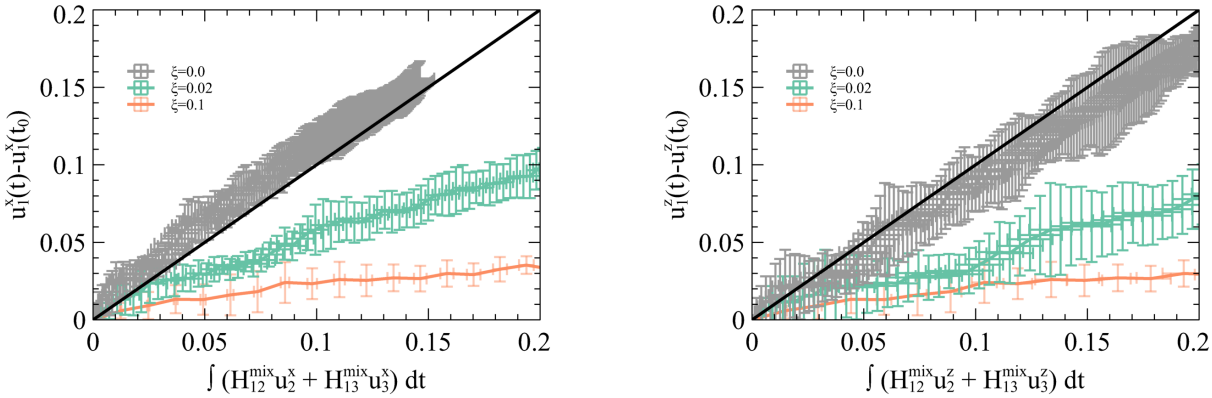

FIG. 9. **Left Panel:** Evaluation of the integral in Eq. (40) after averaging over all bins at different heights. Three values of $\xi = 0.0$ (solid lines), $\xi = 0.02$ (dashed lines), $\xi = 0.1$ (dotted lines) are shown. **Right Panel:** Equivalent evaluation of the z-component of the first eigenvector given by Eq. (42).

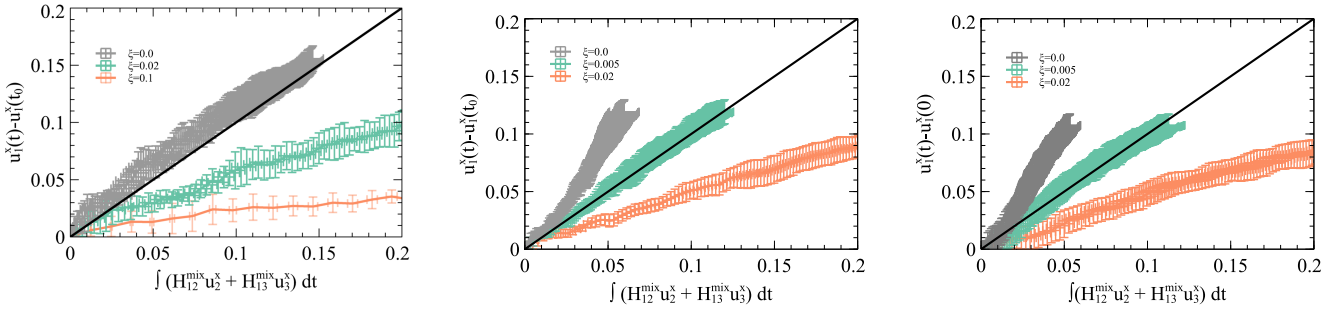

FIG. 10. Evaluation of the integral in Eq. (40) for N=10 increasing concentration w=0.1 (left), 0.5 (center), and 1.0 (right). Eqn (40) is satisfied for ξ=0.005 for both $w = 0.5$ and $w = 1.0$, indicating a plateau in the dependence of ξ with the concentration.

versible parts of Eq. (4) and might overestimate ξ. The ability to separately characterize this effect will allows us to determine the irreversible part of the constitutive modelling via Eq. (19) without spurious effects resulting from a wrong choice in the modelling of the flow kinematics.

VI. CONCLUSIONS

We have analysed the behaviour of polymer solutions modelled microscopically through the SDPD model of fluid particles with some of these particles linked with FENE-P springs. The resulting model fluids mimic polymer chains in solution. The reorientation dynamics upon start-up shear flow has been discussed by using the macroscopic conformation tensor field as observable. For this simple flow, the evolution of the conformation tensor is homogeneous, except for regions very close of the walls where chain depletion occurs. We have introduced an analysis of the evolution of the eigenvectors of the conformation tensor that allows for the separation of non-Newtonian effects resulting from non-affine motion of chains and those resulting directly for the polymeric entropy. Non-affine motion is introduced in the reversible dynamics of the evolution of the conformation tensor through a mixed convected derivative of the Gordon-Schowalter type. In this model, non-affine motion of chains can be quantified through a single parameter: the slip coefficient ξ. Our simulation results show that non-affine motion occurs in these polymeric mesoscopic model fluids. The effects of non-affine motion, measured through the slip coefficient, increase with both the polymer concentration and chain length. The slip coefficients determined from our simulations are small, but using the "slipping" Oldroyd-B model we have demonstrated that a small degree of non-affine motion has significant repercussions for the rheology of the solution.

We hope this work will encourage experimental validation of non-affine motion of chains in the rheological behavior and modeling of complex fluids. Experimental verification of the presence of slip could be achieved through measurement of the orientation of chains in transient flows[41] (i.e., via birefringence measurements). At moderate strain rates, prior to failure of the stress-optic rule,[41,42] birefringence measurements can be used as a proxy for stress measurements. Birefringence measurements have been used in the past to characterize the resistance to chain orientation and its effect molecular weight and polydispersity in the limit of vanishing shear rates.[43,44] The presented approach could be applied, for example, to transient birefringence measurements to character-

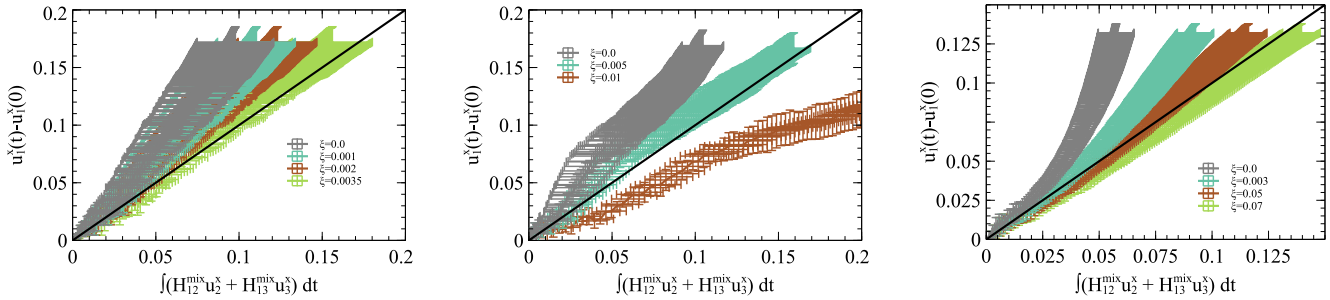

FIG. 11. Evaluation of the integral in Eq. (40) for N=20 and w=0.05 (left), 0.1 (center) and 0.5 (right) averaged over all the heights in the fluid domain as in Figure 9. Equation (40) is satisfied for $\xi > 0.0$ for all concentrations indicating the presence of non-affine deformation and finite slip.

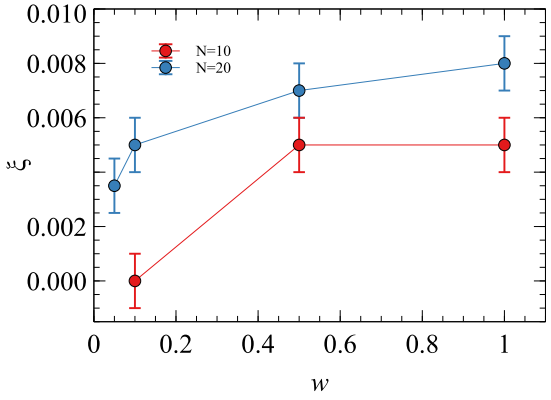

FIG. 12. Slip coefficient ξ as a function of the concentration for fluids with chains N=10 and N=20.

ize the presence of a lag between chain orientation and the inducing flow due to slip.[45,46]

Finally, we highlight that having a method to discriminate independently the different sources of non-Newtonian rheological behaviour through the eigendynamics of the conformation tensor will help produce better data-driven constitutive equations for polymer solutions, where non-affine motion and entropic contributions are clearly separated. Following our method, once the slip parameter is obtained, we can infer $\boldsymbol{\sigma}$ – the entropic contribution to the evolution of $\boldsymbol{c}$ – by using Eq. (19). In this way, simulation (or possibly experimental) data provides the necessary information to learn the closure constitutive equation for the polymeric stress. This two step approach will be the subject of follow up work applying the multiscale scheme presented herein.

ACKNOWLEDGMENTS

This research is supported by the Basque Government through the BERC 2018-2021 program, by the Basque Business Development Agency under ELKARTEK 2022 program (KAIROS project: grant KK-2022/00052), by the Spanish State Research Agency through BCAM Severo Ochoa excellence accreditation SEV-2017-0718, and through projects PID2020-117080RB-C55 ("Microscopic foundations of soft-matter experiments: computational nano-hydrodynamics" and acronym "Compu-Nano-Hydro"), and PID2020-117080RB-C54 ("Coarse-Graining theory and experimental techniques for multiscale biological systems.") funded by AEI - MICIN.

Appendix A: Appendixes

1. Dimensionality in the micro/macro mapping

In the analysis of the micro/macro mapping, we considered whether the determination of the macroscopic coarse-grained variables could be more easily achieved using a projection of the 3D microscopic system into a 2D plane corresponding with the macroscopic domain (i.e., neglecting or setting to zero the components of all vectors and tensors in the neutral direction). To check on this, we analyze the effect of dimensionality on the coupling process. We assume that the conformation tensor evolves according to

$$\dot{\boldsymbol{c}} - \boldsymbol{\kappa}^T\cdot\boldsymbol{c} - \boldsymbol{c}\cdot\boldsymbol{\kappa} = \frac{2}{\lambda_p k_B T}(\boldsymbol{I} - f_d(\mathrm{tr(c)})\mathrm{c}) \tag{A1}$$

where f_d is some arbitrary function of the trace of $\boldsymbol{c}$. This will correspond well to the simple models we have considered before (i.e., Oldroyd-B or FENE-P). As an example we take simple shear and write the system of ODEs for a 3D geometry

$$\dot{c}_{xx} - 2\dot{\gamma}c_{xy} = 1 - f_3 c_{xx} \tag{A2}$$
$$\dot{c}_{xy} - \dot{\gamma}c_{yy} = -f_3 c_{xy} \tag{A3}$$
$$\dot{c}_{xz} - \dot{\gamma}c_{yz} = -f_3 c_{xz} \tag{A4}$$
$$\dot{c}_{yy} = 1 - f_3 c_{yy} \tag{A5}$$
$$\dot{c}_{yz} = -f_3 c_{yz} \tag{A6}$$
$$\dot{c}_{zz} = 1 - f_3 c_{zz} \tag{A7}$$

and a 2D geometry

$$\dot{c}_{xx} - 2\dot{\gamma}c_{xy} = 1 - f_2 c_{xx} \tag{A8}$$
$$\dot{c}_{xy} - \dot{\gamma}c_{yy} = -f_2 c_{xy} \tag{A9}$$
$$\dot{c}_{yy} = 1 - f_2 c_{yy} \tag{A10}$$

From this two sets of ODEs, we can see that equations A2, A3 and A5 are equivalent to A8-A10 only for specific cases like the Oldroyd-B model which has $f_d = 1$). That is, the evolution of each component maintains the same relationship in 3D and 2D. However, for FENE-P $f_d = f(\mathrm{tr}(\boldsymbol{c}))$ and the above is not true since all the equations are coupled with the trace elements of $\boldsymbol{c}$. Therefore, when we map attributes from the microscopic system into the 2D the grid for the macroscopic simulation, we need to consider those as 3D. That is, the conformation tensor $[c]_\mu$ and the velocity gradient $[\nabla \boldsymbol{v}]_\mu$ have to be considered as 3×3 matrices.

2. Planar extension SOB model

To study the limits of the SOB model discussed in the paper, here we present the analytic solution for the conformation tensor components to the SOB model in planar extension.

$$c_{xx} = \frac{1}{1-2(1-\xi)\mathrm{Wi}} \tag{A11}$$

$$c_{yy} = 1 \tag{A12}$$

$$c_{zz} = \frac{1}{1+2(1-\xi)\mathrm{Wi}} \tag{A13}$$

with all the off-diagonal components equal to zero. In Figure 13, we present the first ($c_1 = c_{xx}$) and second ($c_2 = c_{zz}$) eigenvalues of the conformation tensor as a function of the slip coefficient ξ for Wi=0.1 and Wi=0.45. Note, that the diagonal components of $\boldsymbol{c}$ are equivalent to the eigenvalues in extensional flow, but this is not true in shear or complex flows.

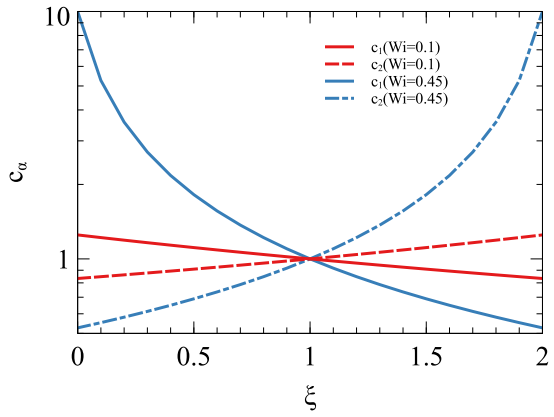

FIG. 13. Analytic solutions for the eigenvalues of the conformation tensor using the "slipping" Oldroyd-B model with $0 \leq \xi \leq 2$ in planar extension.

The evolution of the eigenvalues of $\boldsymbol{c}$ in planar extension can be used to better understand the effect of the slip coefficient across the range $0 \leq \xi \leq 2$. For $\xi = 0$, we recover the UC derivative resulting in the Oldroyd-B model: chains are orienting and stretching in affine motion with the flow. For $0 < \xi < 1$, non-affine motion or slip is observed (i.e., SOB model): chains are still orienting and stretching following the flow but this deformation is not affine. Up to $\xi = 1$, we observe a general tendency for chains to orient with the flow (i.e., $c_{xx} > c_{zz}$). Setting $\xi = 1$ results in the corotational Jaumann-Maxwell derivative and the conformation tensor remains invariant. For $\xi < 1$, chain orientation is reverted and for the limit case of $\xi = 2$ the Oldroyd-A model is recovered. For these last two cases ($\xi > 1$), the solution is inverted and $c_{zz} > c_{xx}$. Therefore, for the description of polymeric solutions only $\xi < 1$ seems appropriate.

References

[1] K. Kremer and F. Müller-Plathe, "Multiscale simulation in polymer science," Molecular Simulation **28**, 729–750 (2002), https://doi.org/10.1080/0892702021000002458.

[2] L. Zhao, Z. Li, B. Caswell, J. Ouyang, and G. E. Karniadakis, "Active learning of constitutive relation from mesoscopic dynamics for macroscopic modeling of non-newtonian flows," Journal of Computational Physics **363**, 116–127 (2018).

[3] J. G. Oldroyd, "On the formulation of rheological equations of state," Proceedings of the Royal Society of London. Series A. Mathematical and Physical Sciences **200**, 523–541 (1950), https://royalsocietypublishing.org/doi/pdf/10.1098/rspa.1950.0035.

[4] R. Bird, P. Dotson, and N. Johnson, "Polymer solution rheology based on a finitely extensible bead—spring chain model," Journal of Non-Newtonian Fluid Mechanics **7**, 213–235 (1980).

[5] N. Phan-Thien and R. I. Tanner, "A new constitutive equation derived from network theory," Journal of Non-Newtonian Fluid Mechanics **2**, 353–365 (1977).

[6] H. Giesekus, "A simple constitutive equation for polymer fluids based on the concept of deformation-dependent tensorial mobility," Journal of Non-Newtonian Fluid Mechanics **11**, 69–109 (1982).

[7] R. J. Gordon and W. R. Schowalter, "Anisotropic fluid theory: A different approach to the dumbbell theory of dilute polymer solutions," Transactions of the Society of Rheology **16**, 79–97 (1972), https://doi.org/10.1122/1.549256.

[8] J. L. Ericksen, "Transversely isotropic fluids," Kolloid-Zeitschrift **173**, 117 (1960).

[9] M. Johnson and D. Segalman, "A model for viscoelastic fluid behavior which allows non-affine deformation," Journal of Non-Newtonian Fluid Mechanics **2**, 255–270 (1977).

[10] M. Johnson and D. Segalman, "Description of the non-affine motions of dilute polymer solutions by the porous molecule model," Journal of Non-Newtonian Fluid Mechanics **9**, 33–56 (1981).

[11] N. Phan-Thien, "A nonlinear network viscoelastic model," Journal of Rheology **22**, 259–283 (1978), https://doi.org/10.1122/1.549481.

[12] J. D. Schieber and A. Córdoba, "Nonequilibrium thermodynamics for soft matter made easy(er)," Physics of Fluids **33**, 083103 (2021), https://doi.org/10.1063/5.0057081.

[13] R. Pivokonsky, P. Filip, and J. Zelenkova, "The role of the gordon–schowalter derivative term in the constitutive models—improved flexibility of the modified xpp model," Colloid and Polymer Science **293**, 1227–1236 (2015).

[14] N. Ramlawi, N. A. Bharadwaj, and R. H. Ewoldt, "The weakly nonlinear response and nonaffine interpretation of the johnson–segalman/gordon–schowalter model," Journal of Rheology **64**, 1409–1424 (2020), https://doi.org/10.1122/8.0000122.

[15] A. Vázquez-Quesada, M. Ellero, and P. Español, "Smoothed particle hydrodynamic model for viscoelastic fluids with thermal fluctuations," Physical Review E **79**, 056707 (2009).

[16] D. Dratler and W. Schowalter, "Dynamic simulation of suspensions of non-brownian hard spheres," Journal of Fluid Mechanics **325**, 53–77 (1996).

[17] H. C. Ottinger, "Complex fluids," in *Beyond Equilibrium Thermodynamics* (John Wiley Sons, Inc., 2005) pp. 97–156.

[18] J. F. Gu and M. Grmela, "Generic model of active advection," Journal of Non-Newtonian Fluid Mechanics **152**, 12–26 (2008), 4th International workshop on Nonequilibrium Theromdynamics and Complex Fluids.

[19]M. Grmela, "GENERIC guide to the multiscale dynamics and thermodynamics," Journal of Physics Communications **2**, 032001 (2018).
[20]A. Beris and B. Edwards, *Thermodynamics of Flowing Systems: with Internal Microstructure*, Oxford Engineering Science Series (Oxford University Press, 1994).
[21]A. N. Beris, "Continuum mechanics modeling of complex fluid systems following oldroyd's seminal 1950 work," Journal of Non-Newtonian Fluid Mechanics **298**, 104677 (2021).
[22]J. L. White, "Dynamics of viscoelastic fluids, melt fracture, and the rheology of fiber spinning," Journal of Applied Polymer Science **8**, 2339–2357 (1964), https://onlinelibrary.wiley.com/doi/pdf/10.1002/app.1964.070080527.
[23]V. Tirtaatmadja and T. Sridhar, "Comparison of constitutive equations for polymer solutions in uniaxial extension," Journal of Rheology **39**, 1133–1160 (1995), https://doi.org/10.1122/1.550632.
[24]L. M. Quinzani, G. H. McKinley, R. A. Brown, and R. C. Armstrong, "Modeling the rheology of polyisobutylene solutions," Journal of Rheology **34**, 705–748 (1990), https://doi.org/10.1122/1.550148.
[25]T. Bodnár and A. Sequeira, "Analysis of the shear-thinning viscosity behavior of the johnson & segalman viscoelastic fluids," Fluids **7** (2022), 10.3390/fluids7010036.
[26]M. Anand, J. Kwack, and A. Masud, "A new generalized oldroyd-b model for blood flow in complex geometries," International Journal of Engineering Science **72**, 78–88 (2013).
[27]A. Souvaliotis and A. N. Beris, "An extended white–metzner viscoelastic fluid model based on an internal structural parameter," Journal of Rheology **36**, 241–271 (1992), https://doi.org/10.1122/1.550344.
[28]M. Kröger, "Simple models for complex nonequilibrium fluids," Physics Reports **390**, 453–551 (2004).
[29]S. Litvinov, Q. Xie, X. Hu, N. Adams, and M. Ellero, "Simulation of individual polymer chains and polymer solutions with smoothed dissipative particle dynamics," Fluids **1**, 7 (2016).
[30]D. N. Simavilla and M. Ellero, "Mesoscopic simulations of inertial drag enhancement and polymer migration in viscoelastic solutions flowing around a confined array of cylinders," Journal of Non-Newtonian Fluid Mechanics , 104811 (2022).
[31]P. Español and M. Revenga, "Smoothed dissipative particle dynamics," Physical Review E **67**, 026705 (2003).
[32]M. Ellero and P. Español, "Everything you always wanted to know about sdpd (but were afraid to ask)," Applied Mathematics and Mechanics **39**, 103–124 (2018).
[33]N. Moreno and M. Ellero, "Arbitrary flow boundary conditions in smoothed dissipative particle dynamics: A generalized virtual rheometer," Physics of Fluids **33**, 012006 (2021), https://doi.org/10.1063/5.0035936.
[34]R. H. Cole, *Underwater explosions* (Princeton University Press,, 1948).
[35]R. Bird, R. Bird, R. Armstrong, and O. Hassager, *Dynamics of Polymeric Liquids, Volume 1: Fluid Mechanics*, Dynamics of Polymeric Liquids (Wiley, 1987).
[36]D. A. Fedosov, G. E. Karniadakis, and B. Caswell, "Steady shear rheometry of dissipative particle dynamics models of polymer fluids in reverse poiseuille flow," The Journal of chemical physics **132**, 144103–144103 (2010).
[37]C. Mo, L. Navarini, F. S. Liverani, and M. Ellero, "Modeling swelling effects during coffee extraction with smoothed particle hydrodynamics," Physics of Fluids **34**, 043104 (2022), https://doi.org/10.1063/5.0086897.
[38]J. A. Backer, C. P. Lowe, H. C. J. Hoefsloot, and P. D. Iedema, "Poiseuille flow to measure the viscosity of particle model fluids," The Journal of Chemical Physics **122**, 154503 (2005), https://doi.org/10.1063/1.1883163.
[39]R. Courant, K. Friedrichs, and H. Lewy, "Über die partiellen differenzengleichungen der mathematischen physik," Mathematische Annalen **100**, 32–74 (1928).
[40]M. Ellero, P. Español, and N. A. Adams, "Implicit atomistic viscosities in smoothed particle hydrodynamics," Phys. Rev. E **82**, 046702 (2010).
[41]C. Luap, C. Müller, T. Schweizer, and D. C. Venerus, "Simultaneous stress and birefringence measurements during uniaxial elongation of polystyrene melts with narrow molecular weight distribution," Rheologica Acta **45**, 83–91 (2005).
[42]M. Kröger, W. Loose, and S. Hess, "Rheology and structural changes of polymer melts via nonequilibrium molecular dynamics," Journal of Rheology **37**, 1057–1079 (1993), https://doi.org/10.1122/1.550409.
[43]J. Bossart and H. C. Oettinger, "Orientation of polymer coils in dilute solutions undergoing shear flow: Birefringence and light scattering," Macromolecules **28**, 5852–5860 (1995).
[44]J. Bossart and H. C. Öttinger, "Orientation of polymer coils in dilute solutions undergoing shear flow: birefringence experiments," Macromolecules **30**, 5527–5540 (1997).
[45]J. Soulages, T. Schweizer, D. Venerus, J. Hostettler, F. Mettler, M. Kröger, and H. Öttinger, "Lubricated optical rheometer for the study of two-dimensional complex flows of polymer melts," Journal of Non-Newtonian Fluid Mechanics **150**, 43–55 (2008).
[46]J. Soulages, T. Schweizer, D. Venerus, M. Kröger, and H. Öttinger, "Lubricated cross-slot flow of a low density polyethylene melt," Journal of Non-Newtonian Fluid Mechanics **154**, 52–64 (2008).